# Accelerated, Memory-Efficient Far-Field Scattering Computation with Monte Carlo SBR

Samuel Audia, Dinesh Manocha, Fellow, IEEE, and Matthias Zwicker, Associate Member, IEEE

This work has been submitted to the IEEE for possible publication. Copyright may be transferred without notice, after which this version may no longer be accessible.

Abstract-We introduce a Monte Carlo integration-based Shooting and Bouncing Ray (SBR) algorithm for electromagnetic scattering, specifically targeting complex dielectric materials. Unlike traditional deterministic SBR methods, our approach is the first to reformulate the SBR integral equations using Monte Carlo techniques and advanced variance reduction strategies adapted from photorealistic rendering. This enables efficient, massively parallel computation on modern GPUs, resulting in up to a 10-15× reduction in memory usage and a 4× speed up in runtime, particularly for multilayer dielectric structures. Our method emphasizes high-energy propagation paths, efficiently capturing long multipath and interreflection effects. Verification on canonical 3D geometries and ISAR imaging of both conducting and dielectric representative aircraft models demonstrates that our Monte Carlo SBR achieves high accuracy while maintaining low noise, making it suitable for downstream imaging and analysis tasks.

Index Terms—IEEE, IEEEtran, journal,  $\LaTeX$ , paper, template.

# I. INTRODUCTION

Modern engineering designs are rooted in computer simulation to vet and iterate performance without costly physical prototypes. In electromagnetic scattering, simulations precisely characterize field propagation, facilitating antenna placement [1]–[4], RADAR analysis [5], [6], and radiation safety verification [7]. Simulations, however, must balance computational speed and fidelity. Full-wave solvers such as Method of Moments (MoM) [8], Finite-Difference Time Domain (FDTD) [9], and Finite Element Method (FEM) [10] solve the full Maxwell's equations but require powerful computational resources and hours to weeks to complete, often restricting their use to electrically small objects.

For objects large relative to wavelength, high-frequency approximation methods offer a practical trade-off. Geometric Optics (GO) [11] traces paths of plane waves and computes surface interactions semi-empirically, but struggles with singularities at caustics and capturing wave effects. Alternatively, Physical Optics (PO) [11] locally approximates currents by the immediate field incident on a planar surface. These currents enable the use of boundary integrals, but struggle to characterize non-convex shapes and multi-path interactions. The Shooting and Bouncing Ray (SBR) method [12], [13] combines GO for incident field propagation and PO for

Samuel Audia, Dinesh Manocha, and Matthias Zwicker are with the University of Maryland, College Park department of Computer Science. Dinesh Manocha is also affiliated with the department of Electrical and Computer Engineering. Correspondence can be sent to sjaudia@umd.edu.

scattered field calculation, and has become the standard for electrically large, complex geometries due to its speed and ease of implementation.

SBR naturally lends itself to hardware acceleration with modern graphics processing units (GPUs) [13]–[15]. Past research, however, has focused on optimizing the standard SBR algorithm through complex ray intersection schemes [15]–[17] and large tree-based ray management [13]. These approaches ignore the underlying hardware, bottlenecking the possible performance. GPUs prefer repeated fixed pipelines to increase overall throughput. Complex ray intersection need to accurately handle double counting when ray tubes overlap adding additional compute and communication overhead for every ray. Tracing both the reflected and refracted rays builds a tree recursively, making it difficult to track the overall memory usage and data dependencies. Furthermore, rays are traced along paths that carry little energy and have a negligible effect on the final result.

In contrast, photorealistic rendering [18], [19], for which GPUs have been optimized, focuses on improving Monte Carlo integration and advanced sampling techniques [20], increasing the overall number of rays while decreasing their individual computation. Monte Carlo methods have been applied to GO ray tracing for wireless coverage mapping [21] and sea surface characterization [22]. They have not, to the authors' knowledge, been used in SBR algorithms that incorporate physical optics currents.

This paper introduces a novel Monte Carlo integration-based SBR algorithm for medium to high fidelity electromagnetic scattering. Our approach departs from traditional deterministic quadrature by randomly sampling paths and integrating over their surface intersections, enabling efficient, trivially parallel computation on GPU hardware. We further adapt advanced samplings techniques from computer graphics to a new SBR context to improve accuracy and efficiency for complex geometries containing dielectric materials. Unlike previous SBR GPU implementations, which require managing large trees of ray intersections, our method aligns with the strengths of GPU hardware to improve scaling of complex scenarios.

Main Results. Our key contributions are:

- A new derivation of the SBR algorithm using Monte Carlo integration and a path space formalism to calculate the scattered field for arbitrary PEC and dielectric objects. Our method and deterministic SBR both converge to the same solution as the number of rays increases.
- Two advanced sampling techniques adapted from computer graphics to SBR: Fresnel-based importance sampling and Russian roulette sampling. We demonstrate the

material objects.

• Implementation and benchmarking of both deterministic and Monte Carlo SBR on GPUs. We benchmark with 3D flat plate, sphere, dihedral, and airplane geometries. Our Monte Carlo SBR algorithm computes results within 1-2dB of average error compared to deterministic SBR, while using 13 to 15 times less memory and 4 times faster runtimes on multi-layer dielectric objects.

# II. BACKGROUND

The Shooting and Bouncing Ray method and Monte Carlo integration are well established in the literature. We provide a brief overview in this section, but for in-depth reviews, we point readers to [13] for SBR and [18] for Monte Carlo integration in computer graphics.

# A. Shooting and Bouncing Ray Method

SBR comprises three main steps: GO ray propagation of plane waves, calculation of PO currents, and surface equivalence calculation of scattered field. A GO wave is described by the polarization and field intensity along a ray direction  $\hat{k}$ . The plane wave along the ray is described by

$$\vec{E} = \vec{E}_0 e^{-jk_0 \hat{k} \cdot \vec{r}},\tag{1}$$

where  $\vec{E}^0$  is a complex vector representing the polarization and intensity,  $k_0$  is the wave number  $(\frac{2\pi f}{c_0})$  for a frequency f and the speed of light in a vacuum  $c_0$ .  $\vec{r}$  is a field point where the plane wave is measured. We assume a factor of  $e^{j\omega t}$  throughout. Equation 1 represents a monochromatic wave. Rays propagate by standard GO laws using perfect reflection and Snell's Law [23] for refracted rays on dielectric boundaries. On PEC boundaries, the internal field is assumed to be 0, so only a reflected ray is traced. Ray intensity is attenuated based on the Fresnel coefficient [23] for the corresponding polarization.

Along boundaries between homogeneous regions, we compute the currents using PO and the Modified Equivalent Current Approximation (MECA) [24], [25]. PO makes the assumption that the current on a surface is only a function of the incident field. In actuality, the current is a difficult to calculate term, influenced by the radiated fields of all other currents on the surface. Regardless, on a PEC surface, the electric PO current is calculated by

$$\vec{J} = 2\hat{n} \times \vec{H}^i, \tag{2}$$

where  $\vec{H}^i$  is the incident magnetic field and  $\hat{n}$  is the surface normal. For a plane wave,  $\vec{H}^i = \hat{k} \times \frac{1}{\eta_0} \vec{E}^i$ , where  $\eta_0$  is the free space impedance. MECA extends this idea to dielectric surfaces using the surface equivalence principle. On the boundary between any two homogeneous regions, the electric,  $\vec{J}$ , and magnetic,  $\vec{M}$ , currents along the boundary can found using

$$\vec{J} = \hat{n} \times \vec{H}$$
 and  $\vec{M} = \vec{E} \times \hat{n}$ . (3)

MECA uses the relations in Equation 3 to approximate the electric and magnetic currents using only the incident,

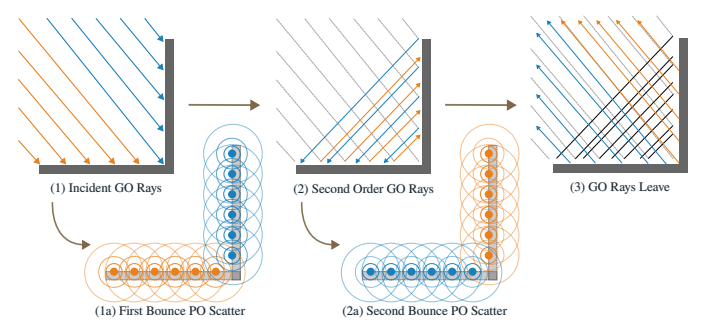


Fig. 1: Core steps of the Shooting and Bouncing Ray method on a perfect electrical conductor dihedral. GO rays are traced orthographically to model a plane wave (1). At each hit, currents are computed and scattered to the far field using the electric field integral equation (1a). Rays reflect to the next surface (2), where currents and scattered fields are again calculated, including phase updates (2a). Rays exit the dihedral and no longer contribute to scattering (3).

reflected, and refracted fields. We denote these fields with i, r, and t superscripts, respectively. Locally, the total field is represented only by the incident GO plane wave; however, we do not consider all three components when scattering and only sum the fields in the region visible to the receiver. In most scattering problems, this will be the outermost surfaces of an object. Interior surfaces have currents associated with them, but these currents do not need to be calculated. This leaves us with two cases to consider: a ray entering the outer surface of an object and a ray exiting the outer surface.

For a ray entering the outer surface, the only *visible* fields are the incident and reflected waves. MECA then approximates the currents as

$$\vec{J} = \hat{n} \times (\vec{H}^i + \vec{H}^r)$$
 and  $\vec{M} = (\vec{E}^i + \vec{E}^r) \times \hat{n}$ . (4)

In the exiting case, only the transmitted field is considered. For completeness, these currents are

$$\vec{J} = \hat{n} \times \vec{H}^t$$
 and  $\vec{M} = \vec{E}^t \times \hat{n}$ . (5)

From the currents on the outer surface,  $\Gamma^o$ , the field can be computed anywhere using the electric and magnetic field integral equation [26]. Often only the far-field scattering is desired, greatly simplifying the calculation. The far-field electric field magnitude in the  $\hat{k}^s$  direction with receiver polarization  $\hat{R}$  is calculated by

$$E^{s}(\vec{k}^{s}, \hat{R}) = jk_{0}\eta_{0} \frac{e^{-jk_{0}r}}{4\pi r} \hat{R} \cdot \int_{\Gamma^{o}} (\hat{k}^{s} \times \hat{k}^{s} \times \vec{J} + \frac{1}{\eta_{0}} \hat{k}^{s} \times \vec{M}) e^{jk_{0}\hat{k}^{s} \cdot \vec{r}'} d\vec{r}', \quad (6)$$

where r is the distance between the local phase center and the observation point.

#### B. Monte Carlo Integration

Monte Carlo integration is invaluable in computing high dimensional and difficult to discretize integrals. Instead of a

$$\int_{\Omega} f(\vec{x}) d\vec{x} = \mathbb{E}_{\vec{x} \sim \mathbf{X}(\Omega)} \frac{f(\vec{x})}{p(\vec{x})}.$$
 (7)

Computing the integral becomes an easier problem of drawing samples from a distribution  $\mathbf{X}$  with support on  $\Omega$ , denoted  $\mathbf{X}(\Omega)$ , and known probabilities  $p(\vec{x})$ . The only requirements are that  $\mathbf{X}$  is easily sampled and  $p(\vec{x})$  is known. The expectation can be approximated by

$$\mathbb{E}_{\vec{x} \sim \mathbf{X}(\Omega)} \frac{f(\vec{x})}{p(\vec{x})} \approx \left( \int_{\Omega} d\vec{x} \right) \frac{1}{N} \sum_{i=1}^{N} \frac{f(\vec{x}_i)}{p(\vec{x}_i)}. \tag{8}$$

As N tends to infinity, the approximation becomes an equality. Convergence of the error is estimated by the squared error, known as the variance. The variance decreases linearly with the number of samples [18], so the error decreases as  $O(n^{-1/2})$ . Common quadrature methods like Newton-Cotes and Gauss-Legendre, have better convergence in lower dimensions [27]; however, as dimensionality increases, the quadrature's time complexity scale grows exponentially, while Monte Carlo integration error remains independent of the dimensionality. For SBR, Monte Carlo integration has little to no benefit for convex PEC shapes. For general shapes with dielectrics, the dimensionality increases with every reflection and refraction, tipping the scales in favor of Monte Carlo integration. We find a runtime improvement of up to 4 times when computing nested dielectric regions (see Table I).

Convergence of Monte Carlo integration can be improved by sampling techniques like stratified sampling, metropolis sampling, or multiple importance sampling. Additional transforms of the integral using control variates can also improve performance. Only stratified sampling and importance sampling is explored in this paper, but by reformulating SBR as a Monte Carlo integration problem, we enable future work on how to improve convergence, much like has been seen in the computer graphics community over the last 25 years. For a broader explanation of Monte Carlo integration in computer graphics, we turn readers to [18].

# III. MONTE CARLO SHOOTING AND BOUNCING RAY METHOD

We start our derivation by considering the SBR scattering integral in path space. From the path space perspective, it is easier to see how each path across multiple bounces contributes to the integral. The integral is then transformed using Monte Carlo integration to establish our method. We build on this novel formulation and consider stratified, Fresnel importance, and Russian Roulette sampling to improve performance.

# A. Fields in Path Space

Consider the path space,  $\mathbb{P}^N$ , instead of traditional 3D Euclidean space,  $\mathbb{R}^3$ .  $\vec{p_i} = (\vec{p_{1,i}}, \vec{p_{2,i}}, \dots, \vec{p_{N,i}}) \in \mathbb{P}^N$  is the  $i^{\text{th}}$  path of length N that connects the transmitter and a scattering surface current (see Figure 2). Each index in the path space

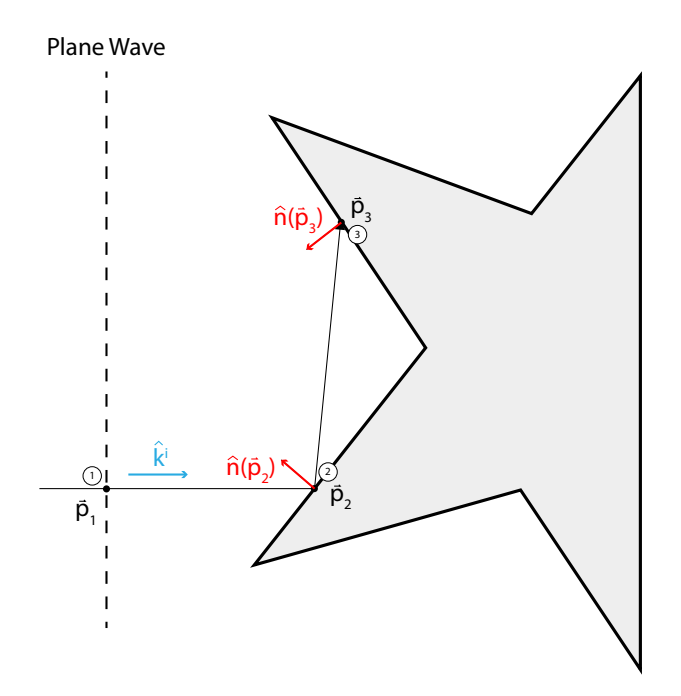


Fig. 2: Depiction of the path space used in our derivation. All rays start at the incident plane wave. Each object intersection adds a new dimension to the path space with corresponding normal  $\hat{n}$  and point  $\vec{r}$ .

corresponds to an intersection with a surface, where  $\vec{p}_{l,i} \in \mathbb{R}^3$  is a 3D point on the object surface for the  $l^{\text{th}}$  intersection and  $\hat{n}(\vec{p}_{l,i}) \in \mathbb{R}^3$  is the corresponding normal. For an incident plane wave with propagation direction  $\hat{k}^i$ , we restrict all path vectors such that  $\frac{\vec{p}_2 - \vec{p}_1}{|\vec{p}_2 - \vec{p}_1|} = \hat{k}^i$ . As we are only considering the scattered field, we do not consider direct paths from the transmitter to the receiver and consider only  $\mathbb{P}^N | N > 1$ .

The path space is useful because we can more easily represent the electric and magnetic fields along each ray. We briefly drop the index i for legibility. Along each path we care about two quantities: the phase,  $\phi(\vec{p}) \in \mathbb{C}$ , and the field polarization and intensity,  $\vec{E}_0(\vec{p}) \in \mathbb{C}^3$ . These quantities are defined over the full path that the field takes. Phase is a function of the total distance traveled and the medium in which the field propagates. For each segment of the path, the propagation is scaled by the relative permittivity,  $\epsilon_r$ , and permeability,  $\mu_r$ , with an index of refraction of  $n_l = \sqrt{\epsilon_{r,l}\mu_{r,l}}$ . The overall phase is then

$$\phi(\vec{p}) = \sum_{l=1}^{N-1} n_l |\vec{p}_{l+1} - \vec{p}_l|. \tag{9}$$

If the transmitter is in the near field, then Equation 9 holds; however, we want to calculate currents from an incident plane wave, effectively placing the transmitter at infinity, producing an infinite phase term. Instead, the first phase calculation is relative to a phase center placed at the center of the object's coordinate system. The resulting phase is

$$\phi(\vec{p}) = n_1 \vec{k}^i \cdot \vec{p}_1 + \sum_{l=2}^{N-1} n_l |\vec{p}_{l+1} - \vec{p}_l|.$$
 (10)

As the electric and magnetic fields propagate together in a plane wave, their phases are the same along the total path. The field intensities and polarizations are also easy to track. Let  $\vec{E}_0$  be the polarization and intensity of the incident plane wave. When the field interacts with surfaces, the field splits, scales, and rotates based on the Fresnel equations for the p and s polarizations. To track both reflected and refracted paths we introduce an additional function

$$\mathbf{f}(\vec{p}_{l-1}, \vec{p}_l, \vec{p}_{l+1}) = \delta^r(\vec{p}_{l-1}, \vec{p}_l, \vec{p}_{l+1}) \mathbf{T}^r(\vec{p}_{l-1}, \vec{p}_l, \vec{p}_{l+1}) + \delta^t(\vec{p}_{l-1}, \vec{p}_l, \vec{p}_{l+1}) \mathbf{T}^t(\vec{p}_{l-1}, \vec{p}_l, \vec{p}_{l+1}), \quad (11)$$

where  $\delta^r$  is nonzero only when the exiting direction,  $\frac{\vec{p}_{l+1} - \vec{p}_l}{|\vec{p}_l + 1 - \vec{p}_l|}$ , is the perfect reflection of the incident direction,  $\frac{\vec{p}_{l+1} - \vec{p}_{l-1}}{|\vec{p}_l - \vec{p}_{l-1}|}$ . Similarly,  $\delta_t$  is only nonzero when the vectors satisfy Snell's law. The 3 by 3, complex valued transformation matrices  $\mathbf{T}^r$  and  $\mathbf{T}^t$  then apply the Fresnel coefficients to the incident field. On PEC surfaces only the reflected term is present. Equation 11 uses a three point form to describe the relationship between the incident ray and exiting ray directions by the points that make up the two vectors. By using points instead of normalized vector directions, we can more easily integrate and sample surfaces. The full expression for the GO field with respect to its path  $\vec{p}$  is

$$\vec{E}(\vec{p}) = (\prod_{l=2}^{N-1} V(\vec{p}_{l+1}, \vec{p}_l) \mathbf{f}(\vec{p}_{l-1}, \vec{p}_l, \vec{p}_{l+1}))$$

$$\mathbf{T}(\vec{p}_{N-1}, \vec{p}_N) \vec{E}_0 e^{-jk_0 \phi(\vec{p})}. \quad (12)$$

The final matrix  $\mathbf{T}(\vec{p}_{N-1},\vec{p}_N)$  is a special case. As described in the background, we only consider the field visible to the receiver when scattering. Therefore, the final transformation is simply a function of the vector from  $\vec{p}_{N-1}$  to  $\vec{p}_N$  and the surface normal at  $\vec{p}_N$ . Depending on the orientation of the ray and surface normal, the matrix could represent either the reflected or refracted field. No additional ray splitting occurs at the final point in the path. The additional  $V(\vec{p}_{l+1}, \vec{p}_l)$  term is 0 when the two points are occluded from one another and 1 otherwise.

Finally, the magnetic field is simply the scaled field orthogonal to the propagation direction and electric field polarization. When considering lossy materials, the propagation of the GO ray is slightly more complicated [13]. We use the simpler equations in our derivation, but the extension is straightforward.

# B. Scattering Integral in Path Space

We calculate the scattered field using Equation 12 and Equations 3, 4, 5, and 6. Far-field scattering only considers the currents on the outermost surface which are visible to the receiver. We define a characteristic function  $\chi(\vec{p}_N)$  to only consider these currents. To clarify Equation 6's reliance on previous path points, we express the equation as a series of

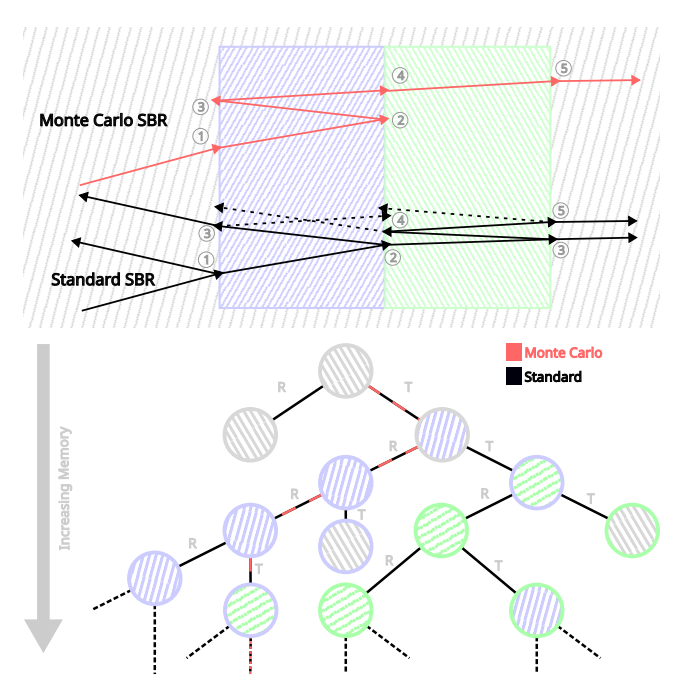


Fig. 3: Visual comparison between deterministic and Monte Carlo integration of dielectric regions. The deterministic algorithm must build a large tree to search the whole space, while the Monte Carlo algorithm must only walk a subset of the possible paths to calculate the scattering.

nested integrals. For all rays of path length N starting at the initial plane wave,  $\Gamma_1$ , the scattered field is

$$E_{N}^{s}(\vec{k}^{s}, \hat{R}) = jk_{0}\eta_{0} \frac{e^{-jk_{0}r}}{4\pi r} \hat{R} \cdot \int_{\Gamma} \cdots \int_{\Gamma} \int_{\Gamma_{1}} \chi(\vec{p}_{N})$$

$$\frac{(\hat{k}^{s} \times \hat{k}^{s} \times \vec{J}(\vec{p}) + \frac{1}{\eta_{0}} \hat{k}^{s} \times \vec{M}(\vec{p}))}{|\hat{k}_{N}^{r} \cdot \hat{n}(\vec{p}_{N})|} e^{jk_{0}\hat{k}^{s} \cdot \vec{p}_{N}}$$

$$d\vec{p}_{1} \cdots d\vec{p}_{N-1} dA(\vec{p}_{N}). \quad (13)$$

After the initial plane wave, all surfaces of the object, denoted by  $\Gamma$ , are integrated. The final integral basis is also changed to transform the plane wave given by Equation 12 in to a surface integral over the currents. This transformation introduces a change of basis factor given by  $\frac{1}{|\hat{k}_N^r \cdot \hat{n}(\vec{p}_N)|}$ , where  $\hat{k}_N^r = \frac{\vec{p}_N - \vec{p}_{N-1}}{|\vec{p}_N - \vec{p}_{N-1}|}$ . Note that the denominator of this scale term can never be zero because that would imply that the ray and surface are parallel. In which case, no surface intersection occurs.

Equation 13 is written such that intermediate path spaces are continuous; however, SBR only traces reflected and transmitted rays as shown in Equation 11. As such, we reduce the degrees of freedom and transform the integrals into sums. These sums are over either one or two elements depending on if the surface is pec or dielectric, respectively. These choices build a tree like structure of possible ray paths as visible in Figure 3. There is also only a single choice for  $p_2$  given  $p_1$  because the incident direction is fixed. The scattering point  $p_N$  is similarly fixed by the previous points in the path space.

Each ray path, therefore, has a maximum of  $2^{N-2}$  possible configurations. The simplified scattered field equation is then

$$E_{N}^{s}(\vec{k}^{s}, \hat{R}) = jk_{0}\eta_{0}\frac{e^{-jk_{0}r}}{4\pi r}\hat{R} \cdot \sum_{1}^{\infty} \cdots \sum_{N=1}^{\infty} \int_{\Gamma_{1}} \chi(\vec{p}_{N}) \frac{(\hat{k}^{s} \times \hat{k}^{s} \times \vec{J}(\vec{p}) + \frac{1}{\eta_{0}}\hat{k}^{s} \times \vec{M}(\vec{p}))}{|\hat{k}_{N}^{r} \cdot \hat{n}(\vec{p}_{N})|} e^{jk_{0}\hat{k}^{s} \cdot \vec{p}_{N}} dA(\vec{p}_{1}). \quad (14)$$

We transform the integral basis over  $p_1$  to the area equivalent; however, no new factor is introduced because the initial ray direction is inline with the plane wave normal by definition. Equation 14 can be interpreted as integrating across all rays that reach the outer surface on their  $N^{th}$  interaction.

For non-convex shapes and those containing materials, a path may intersect the outer surface multiple times. As such, we must consider paths of all lengths and the full scattered field is given by

$$E^{s}(\vec{k}^{s}, \hat{R}) = \sum_{l=2}^{\infty} E_{l}^{s}(\vec{k}^{s}, \hat{R}).$$
 (15)

The combination of Equations 14 and 15 fully characterizes the scattered field computed by the SBR algorithm. The novel path space interpretation of the SBR integral highlights the difficult scaling of the algorithm. As longer and longer path lengths are considered,  $2^{N-2}$  grows exponentially. We depict this growth for two dielectric regions sharing a single boundary in Figure 3. The deterministic SBR algorithm must trace all of these growing number of paths, while our Monte Carlo method only explores a single path.

#### C. Monte Carlo Integration of Scattering

Equation 15 can be computed either using Riemann integration [13] or with our method using Monte Carlo integration. Previous works required the tracing of all paths. This requires difficult tracking of beam areas and complicated field discretization schemes [15], [16]. Instead, our method simplifies the computation for each ray and does not require tracking multiple inter-reflections in dielectric mediums. Our method can result in more overall rays being traced; however, the lack of stack is easier to parallelize on GPU hardware, often resulting in better performance.

Applying Monte Carlo integration to Equation 14 results in

$$E_{N}^{s}(\vec{k}^{s}, \hat{R}) = jk_{0}\eta_{0} \frac{e^{-jk_{0}r}}{4\pi r} \hat{R}.$$

$$\mathbb{E}_{\vec{p}\sim\mathbb{P}^{N}} \frac{\chi(\vec{p}_{N})}{p(\vec{p})} \frac{(\hat{k}^{s} \times \hat{k}^{s} \times \vec{J}(\vec{p}) + \frac{1}{\eta_{0}}\hat{k}^{s} \times \vec{M}(\vec{p}))}{|\vec{k}_{N}^{r} \cdot \hat{n}(\vec{p}_{N})|}$$

$$e^{jk_{0}\hat{k}^{s} \cdot \vec{p}_{N}}, \quad (16)$$

where  $p(\vec{p})$  is the probability of the sampled path. Herein lies the benefit of our method. If we are able to sample, with a known probability, rays that contribute the most to the scattered field, we can improve the performance of the SBR

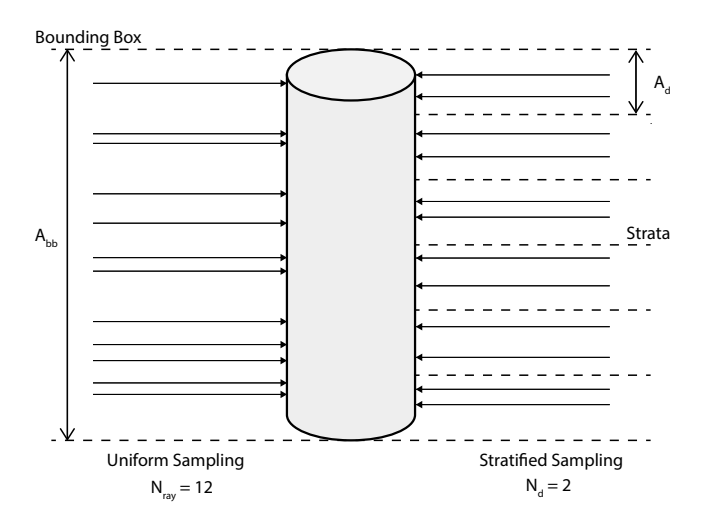


Fig. 4: Comparison between uniform (left) and stratified (right) sampling. Uniform sampling can produce unexpected cluster of samples. Stratified sampling mitigates the issue by uniformly sampling in subdivisions called strata. In SBR this allows the algorithm to more easily sample the oscillations of induced currents.

algorithm. The probability of the full path is the product of the probability at each path segment, giving

$$p(\vec{p}) = \prod_{l=1}^{N} p(\vec{p}_l).$$
 (17)

For PEC reflections, there is only one possible path the ray can take with a probability of 1. Equation 16 is then discretized for numerical integration, giving

$$E_{N}^{s}(\vec{k}^{s}, \hat{R}) \approx jk_{0}\eta_{0} \frac{e^{-jk_{0}r}}{4\pi r} \frac{\int_{\Gamma_{1}} dA(\vec{p}_{1})}{N_{s}} \hat{R} \cdot \sum_{i=1}^{N_{s}} \frac{\chi(\vec{p}_{N,i})}{p(\vec{p}_{i})} \frac{(\hat{k}^{s} \times \hat{k}^{s} \times \vec{J}(\vec{p}_{i}) + \frac{1}{\eta_{0}} \hat{k}^{s} \times \vec{M}(\vec{p}_{i}))}{|\vec{k}_{N,i}^{r} \cdot \hat{n}(\vec{p}_{N,i})|} e^{jk_{0}\hat{k}^{s} \cdot \vec{p}_{N,i}}, \quad (18)$$

where  $N_s$  is the number of paths sampled and  $\int_{\Gamma_1} dA(\vec{p_1})$  is the sampled cross-sectional area of the incident plane wave. To compute each term of the infinite sum in Equation 15, the path from the previous term is extended by tracing another ray. This approach removes the need to recalculate existing paths without biasing the estimator. Two factors contribute the most to the path in SBR: the initial ray launch location and dielectric interactions. In the following subsections, we discuss how to compute the initial distribution and advanced sampling methods to improve performance of our method.

# D. Stratified Sampling

For the initial ray launch, a bounding box is calculated around the object by projecting the computational mesh on the plane orthogonal to the incident ray. Ray starting positions are then sampled from this 2D rectangle. If sampled uniformly, the probability of each ray is simply one over the area of

the bounding rectangle,  $A_{bb}$ . In our implementation, we found that simple uniform sampling produced results that were too noisy compared to the deterministic algorithm. To mitigate the problem, we apply stratified sampling [18].

Instead of every ray sampling from the whole bounding box, the box is first subdivided into strata. Each stratum is sampled  $N_d$  times and has an area of  $A_d = \frac{A_{bb}}{N_s/N_d}$  (Figure 4). As an analog to computer graphics, imagine the plane wave is discretized into pixels. Each pixel is sampled independently. The size of these individual strata along with their sampling is explored in Subsection IV-B. Finer sampling improves integration of the surface current oscillations, and we find that strata on the order of a wavelength perform best.

# E. Fresnel Importance Sampling

Unlike in deterministic SBR, Monte Carlo SBR picks a single reflected or refracted ray at each dielectric boundary instead of tracing both. This removes the need to build a tree of paths, simplifying the algorithm and making SBR trivially parallelizable as all path contributions are independent without needing to backtrack. Monte Carlo implementations have flexibility in how they choose the reflected or refracted path. A simple option is give each a direction a probability of 0.5; however, this ignores the relative energy along the two paths. For example, a ray entering glass from air at normal incidence will reflect with a twentieth of the power. The rest in transmitted into the medium. Intuitively we want to sample along rays which carry the most energy. Doing so is easily accomplished by adjusting the probabilities at the dielectric boundaries based on the computed Fresnel coefficients. For our implementation, we set the probability of a reflected ray to the averaged Fresnel coefficient,  $\bar{R}$ , for each polarization giving

$$\bar{R} = \frac{|r_s| + |r_p|}{2}. (19)$$

The probability of refracted rays is  $1-\bar{R}$ . There are two important characteristics of this probability. First, we purposely chose to use Fresnel coefficient directly instead of ray power because the square in the power often oversamples the reflected or refracted path. For example, in the air to glass example above, the power is 0.04 while  $\bar{R}$  is 0.2. Second, the reflection coefficients must be used because they are bounded between 0 and 1. Transmission coefficients can be greater than 1 when transitioning into a medium with a lower index of refraction. Using reflection coefficients also more easily aligns with PEC surfaces where the reflection coefficient is always 1. The effect of this sampling technique is explored in Section IV-D1.

#### F. Russian Roulette Sampling

Equation 15 shows that we must consider path lengths up to infinity. If we simply terminated the ray at a set number of bounces, then the Monte Carlo integration would be biased and converge to a different integral value. In practice, however, we will need to set a maximum bounce limit. Ideally we can set this limit to a very high value to reduce the error, but at the same time, we do not want to trace long paths

that have little energy, increasing runtime. We use Russian roulette sampling to kill off rays with little energy and average their contribution into the other rays. Before adding another segment to each path, a probability distribution is randomly sampled to determine whether to continue. This decision is determined by a threshold  $q \in (0,1)$ . By convention, if the drawn value is greater than q, then the path continues. To not introduce bias into the integral, all rays that continue are weight by  $\frac{1}{1-q}$ . In our work, we set q=0.5 and draw from a uniform distribution. Therefore, continuing each path is, in effect, a coin flip. Future work could explore different cutoffs and sampling distributions. The effect of Russian Roulette sampling is explored in Section IV-D2.

#### G. Hardware Alignment

For GPU parallelization, SBR algorithm has two main alternating stages (Figure 1): the trivially parallel ray trace to compute PO currents from the GO field and the reduction to calculate the scattered field. Ray-surface intersections have been extensively studied and optimized. Generally, an acceleration structure like a k-d tree [28] or bounded volume hierarchy (BVH) [29] is used to reduce the number of triangles that need to be queried. From there, a simple  $3 \times 3$  linear equation is solved for each triangle to check for ray intersection. This traversal and intersection calculation are what the application specific integrated circuits (ASIC) ray tracing cores compute. General computation, such as computing currents or new ray directions, are executed on the general GPU compute cores with no ASIC improvements. There is little difference in the these steps between the Monte Carlo and standard SBR algorithms. What does change is removal of a call stack for dielectric paths. The standard algorithm traces all reflected and refracted paths until the path energy drops below a certain threshold. This traversal is similar to a depth first search and requires the construction of a stack to save the field's state at each junction. The stack adds additional memory overhead to the ray trace, limiting the length of paths. The varying execution paths also cause divergence between GPU threads, lowering throughput as groups of threads must execute the same instruction. If too many adjacent operations differ, then GPU threads can be left inactive waiting their turn. The Monte Carlo integration algorithm, in contrast, does not require saving the field state at junctions because it simply picks one of the paths and proceeds. This simplicity makes it easy to implement an iterative ray tracer and enable greater throughput.

The reduction step can be difficult to parallelize on the GPU as it requires communication between threads. The recursive nature of the deterministic algorithm makes it difficult to predetermine the data access patterns of the algorithm. The Monte Carlo algorithm, in contrast, uses a fixed number of paths per GPU call. As such, the communication and memory write overhead can be better amortized by coalescing nearby loads and stores. Overall, the Monte Carlo algorithm is easier to vectorize than the deterministic algorithm by advancing a wavefront of rays without needing to backtrack.

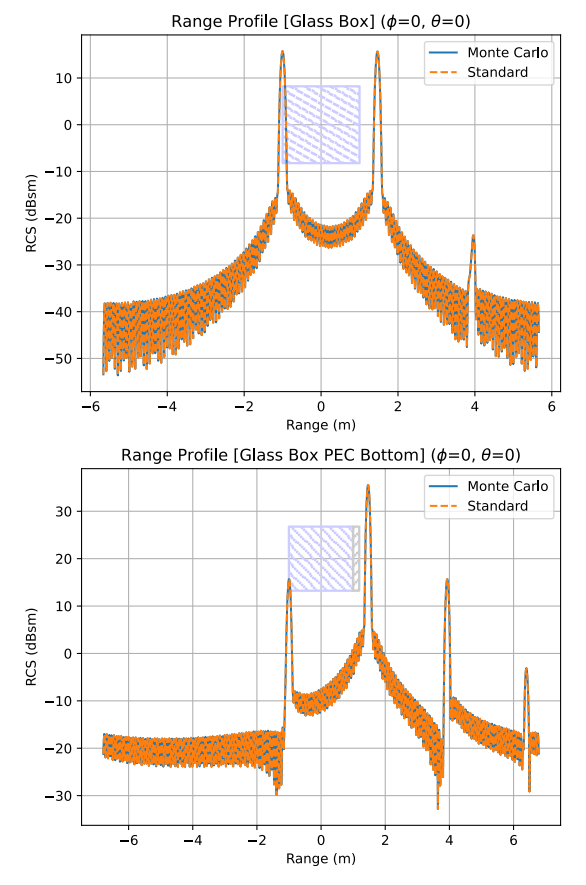


Fig. 5: Range profile correctness for dielectric cubes with and without PEC backing. The peaks match between deterministic and Monte Carlo SBR on multiple interreflections and scattering of the field.

#### IV. RESULTS

We evaluate the performance of our Monte Carlo SBR algorithm against deterministic SBR on a variety of 3D benchmarks including: a flat plate, a sphere, a box, a dihedral, a nested dielectric, and an airplane. We also investigate the effect of Fresnel splitting and Russian roulette sampling on dielectric materials. Suitability for downstream signal processing is demonstrated with inverse synthetic aperture RADAR (ISAR) images of a PEC and dielectric airplane geometry.

We use the Mitsuba [30] retargetable renderer to implement both methods. Mitsuba has been used extensively in computer graphics research [31]–[33], and provides Fresnel equations and ray triangle intersections. The renderer is build on top of Dr. Jit [34] which uses just-in-time compilation to optimize the solver and execute on GPU hardware using CUDA [35] and OptiX [14], [36]. Our implementation is not simply a direct application of Mitsuba, which does not currently support surface current calculation or physical optics integration. We rather, implemented our own render and utilized the lower level functionality such as GPU dispatch and random number generation. All experiments are run using an RTX 2070 super GPU with 8 GB of video memory.

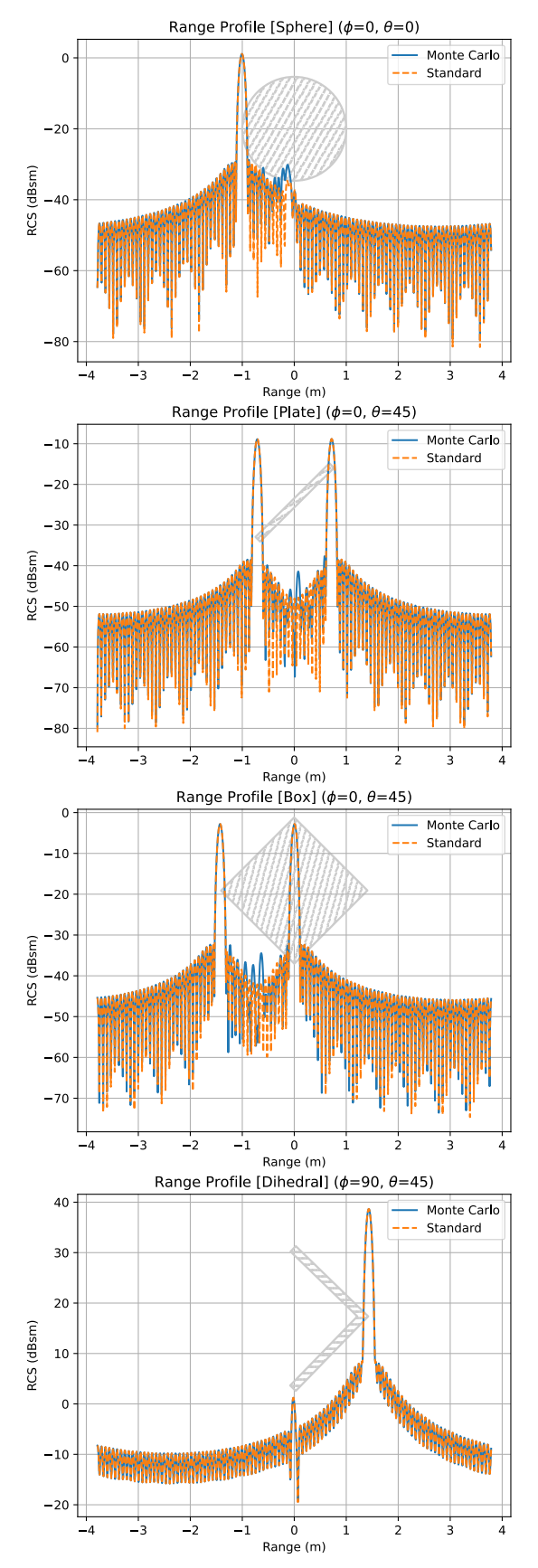


Fig. 6: These range profiles compare the correctness of the deterministic and Monte Carlo SBR algorithms. We see that peaks align at the expected range location with little noise introduced by the random sampling.

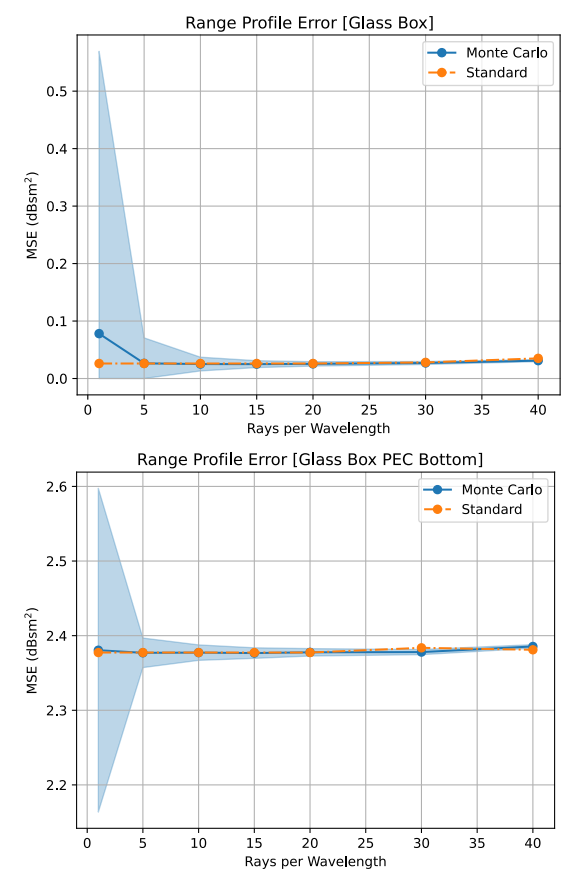


Fig. 7: Error in dB space across 100 runs of the Monte Carlo algorithm as a function of the average number of rays per wavelength. As expected, as the number of rays increases, the deterministic and Monte Carlo algorithms converge to the same answer. Ground truth is given by the analytical solution.

# A. Correctness

We begin by showing that the deterministic SBR algorithm and our Monte Carlo SBR algorithm converge to the same results and produce the same range profile for PEC and dielectric objects. Range profiles are constructed by taking the inversefast-Fourier transform of the frequency data and scaling by the speed of light in a vacuum. The square root radar cross section (RCS) of the field,  $\sqrt{\sigma} = \lim_{r \to \infty} 2\sqrt{\pi} r \frac{\vec{E}^s}{|\vec{E}^i|}$ , is used to push the receiver location to infinity while maintaining complex phase information. Range profiles are highly dependent on the continuity, amplitude, and phase of the computed field across multiple frequencies demonstrating our methods suitability for common radar processing algorithms. Additionally, range profiles provide easy to visualize comparisons with clear connections with the underlying geometry. Peaks correspond to scattering features like current discontinuities and specular reflections.

Frequencies between 1 and 3 GHz were computed with a 20 MHz step size. The sphere, plate, cube, and dihedral are modelled as PEC. The glass cubes are represented as bulk materials with  $\epsilon_r=1.5$ . We set the ray density to  $\frac{\lambda}{40}$  in the deterministic algorithm and stratified beams to  $\frac{\lambda}{10}$  with 16 samples in each stratum. The VV response is considered in

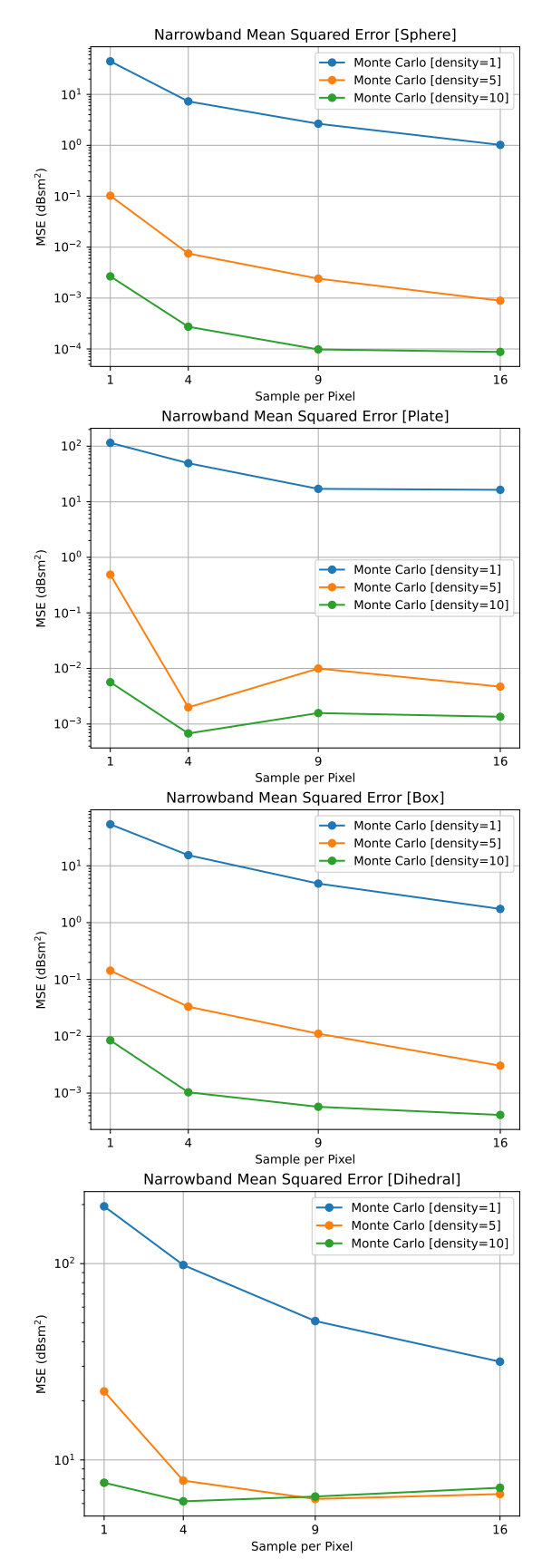


Fig. 8: Error convergence versus sampling density for VV narrowband sweeps of various geometries. Strata area strongly influences performance, with in-beam sampling providing additional refinement.

all plots, corresponding to the polarization of the receiver and transmitter, respectively. Both algorithms are using the same overall number of rays. We use a simple midpoint rule for integrating over the beam area in the classic algorithm. Our method compares favorably to the standard algorithm (Figure 5 and 6).

For the dihedral, the glass cube, and the PEC backed glass cube, the two techniques are line for line. The sphere, plate, and PEC cube, match at the peaks, but there is some additional noise in the Monte Carlo solution. These regions correspond to parts of the object that need to cancel adjacent sources in phase. This additional noise is the main drawback of the Monte Carlo integration method; however, the noise can be easily lowered by taking more samples. We also do not believe that this noise will hinder downstream processing.

#### B. Convergence

Convergence is explored by computing the mean squared error of narrowband plots for the sphere, plate, PEC box, and dihedral swept from 0 to 90 degrees in  $\theta$ . The error is computed relative to the deterministic method solved with a density of  $\frac{\lambda}{60}$ . We compute the VV response at 101 frequencies from 1 to 3 GHz. The equivalent deterministic algorithm ray density can be computed as  $density \cdot \sqrt{samples\ per\ pixel}$ . Figure 8 shows that by increasing the strata ray density, the error is greatly reduced, while increasing the number of samples taken within each sub beam decreases error by a smaller magnitude. From these results, we recommend sizing the strata areas to 10 rays per wavelength and draw multiple samples within these sub beams as needed.

For the dielectric cubes, we are able to compare range profiles to the analytical solutions at normal incidence by matching the phases at each boundary and computing the scattering. Figure 7 shows the prediction error of the standard and Monte Carlo algorithms as compared to the exact solution. To characterize the Monte Carlo estimate, we average the error across 100 initial seed values and plot the mean and first standard deviation. When sampling with very low ray densities, the variability of the Monte Carlo estimate is high with swings of up to  $0.5 \ dBsm^2$ ; however, once at least 10 rays per wavelength are sampled, the variance is greatly reduced, and the two algorithms are within  $0.01 \ dBsm^2$  of error. We have demonstrated that our method is able to converge to a reasonable answer using a comparable number of rays as the standard algorithm.

# C. Runtime and Memory Usage

For objects containing dielectric surfaces, especially multiple stacked dielectric surfaces, our approach greatly reduces both memory and runtime (See Table I). We compare the performance of computing a single monostatic response at normal incidence for both of our glass cubes (Figure 5) and a nested diamond and glass cube with PEC sphere in the center (Figure 9). All three objects are symmetric with respect to vertical and horizontal polarization. The nested cube evaluates performance on objects with multiple interreflections and complex field paths. 101 frequencies from 1 to 3 GHz

TABLE I: Runtime and memory comparison of Monte Carlo and standard SBR methods on various dielectric shapes, using 20 samples per wavelength. Runtimes are averaged over 10 runs (plus 3 warmup runs for GPU kernel caching). All dielectric shapes benefit from lower memory usage, while nested dielectrics show improved runtime. Dr. Jit employs a copy-on-write optimization, given in parentheses, which is challenging to replicate in lower-level code. SBR memory usage is characterized by forcing allocation at each material boundary and reporting both values.

	Monte Carlo (ours)		Deterministic	
Units	s ↓	MiB ↓	s ↓	MiB ↓
Glass Cube	$2.47 \pm 0.01$	10.8	$2.70 \pm 0.08$	128.3 (19.3)
PEC Bottom	$2.78 \pm 0.02$	12.0	$2.52 \pm 0.08$	128.3 (19.3)
Nested	$2.82 \pm 0.02$	24.2	$11.0 \pm 0.10$	348.2 (88.8)

were computed. Monte Carlo used 10 strata per wavelength, with 4 samples in each area, and the standard algorithm used an equivalent ray density of 20. Both used a fixed max bounce count of 9. Runtimes were averaged across 10 trials, with 3 warmup runs to allow for Dr. Jit to cache the GPU kernels. Peak GPU memory usage was reported by Dr. Jit.

For the deterministic solver, two values are given for memory. Dr. Jit uses a copy-on-write optimization to allocate more memory only when a buffer is written. For single region, convex dielectrics, this can greatly reduce the memory usage as the rays quickly leave the scene. Such optimizations, however, are difficult in optimized code not using a higher level library. As such, we force Dr. Jit to allocate the necessary stack memory at each material boundary to characterize what a typical SBR implementation, without this optimization, would use. Both numbers are reported, but even with this optimization, our method still requires half the memory.

First comparing glass cubes, we see little difference in runtime because there are no complex interaction between dielectric surfaces in the object. The ray state tree (Figure 3) for these objects is degenerate, as rays leaving do not reflect back. In both methods, the number of rays traced is linear with the path length; however, even in this simple case, we see large improvements in the memory usage. The standard algorithm cannot, in general, tell that this degenerate tree structure will form, so it must save the state of the rays at each hit and trace both the reflected and transmitted rays. This leads to a memory growth exponential in the number of paths. By using less memory, larger scenes can fit on a GPU and longer, more complex multipath effects can be calculated. The nested cube also sees a similar order of magnitude improvement in memory usage, but also realizes a 4 times speed up in runtime. For the nested cube, the state tree looks more similar to the tree shown in Figure 3. The Monte Carlo algorithm does not need to trace each individual path like the standard algorithm needs to, resulting in a faster solver. Using techniques like Fresnel and Russian roulette sampling, as explored in the next section, the Monte Carlo algorithm is able to reduce the necessary computation even further.

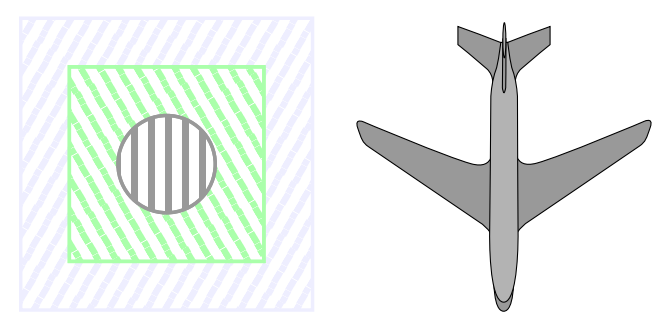


Fig. 9: Illustration of test geometries: Left, a layered dielectric cube (3 m,  $\epsilon_r=1.5$ ) with an inner cube (2 m,  $\epsilon_r=2.0$ ) and a PEC sphere (0.5 m radius). Right, a representative PEC airplane with 7 m wingspan and body length, and a 1.5 m tail fin.

# D. Sampling

1) Fresnel Sampling: We propose using a ray split probability based on the average reflection coefficient calculated by the Fresnel equation instead of a simple 50/50 split. We compare performance on the two glass cubes (Figure 5) and nested dielectric geometry (Figure 9). For the glass cubes, we compute the error relative to the analytical solution, while for the nested cubes, we compare against the standard algorithm with a ray density of 40 rays per wavelength. We again average across 100 seed values and plot both the mean and first standard deviation. The solid line and area are the Fresnel sampling results, and the dashed line and hatched area are the 50/50 sampling results. Results are plotted in Figure 10.

For the glass cube, we find that the Fresnel sampling actually performs worse than the 50/50 sampling with higher variance, especially at lower ray densities. This difference is due to the fact that the reflection coefficient is on the order of 0.101 and most of the wave's energy leaves the cube on every bounce. We, however, need to compute long interreflections so need to trace many internally reflecting rays. The PEC backed cube performs better because the metal plate forces these reflections. Even with the help, the Fresnel sampling performs worse than the 50/50 sampling. Fresnel sampling begins to improve performance on the nested cubes. Because rays do not quickly leave the scene, the sampling follows scattering rays that quickly leave the inner layers and scatter on the outer surface. Though Fresnel sampling does not improve performance in all scenarios, many objects will have multiple dielectric regions where the technique performs best.

2) Russian Roulette Sampling: We also propose using Russian roulette sampling to truncate long paths by probabilistically killing rays. These long paths arise from large interreflections common in dielectric materials, though certain PEC geometries can produce many bounces as well. After a minimum number of bounces, 2 for the glass and pec backed cubes and 6 for the nested cubes, we begin sampling from a uniform distribution to test if the ray should be killed based on a fixed probability of 0.5. Though this sampling technique introduces slight variance in the estimator, we expect to see an improvement in speed as long paths are removed early.

Figure 11 represents the active ray count by the bar graph

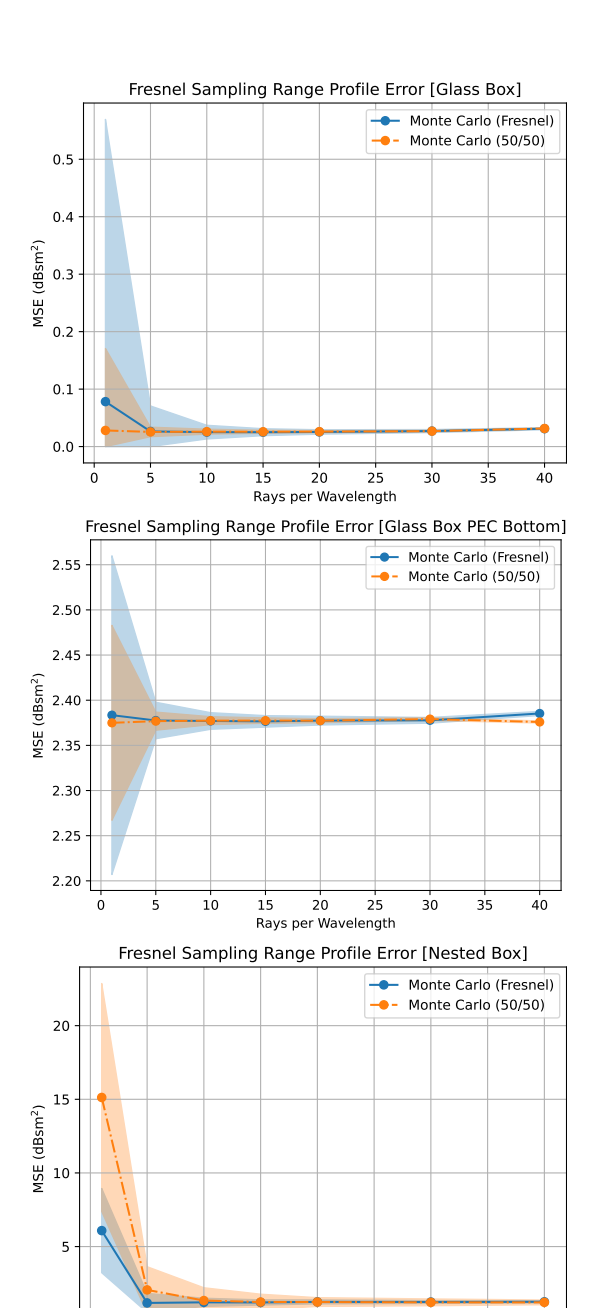


Fig. 10: Fresnel sampling performance on three cube configurations: dielectric, PEC-backed dielectric, and nested dielectric. Errors are averaged over 100 seeds, with mean and first standard deviation shown. Solid lines/areas denote Fresnel sampling; dashed/hatched regions indicate 50/50 splitting. Fresnel sampling underperforms for single dielectrics due to high transmission losses, but excels in nested dielectrics by emphasizing significant paths. This suggests Fresnel sampling remains effective for complex, realistic objects with multiple dielectric regions.

20

25

10

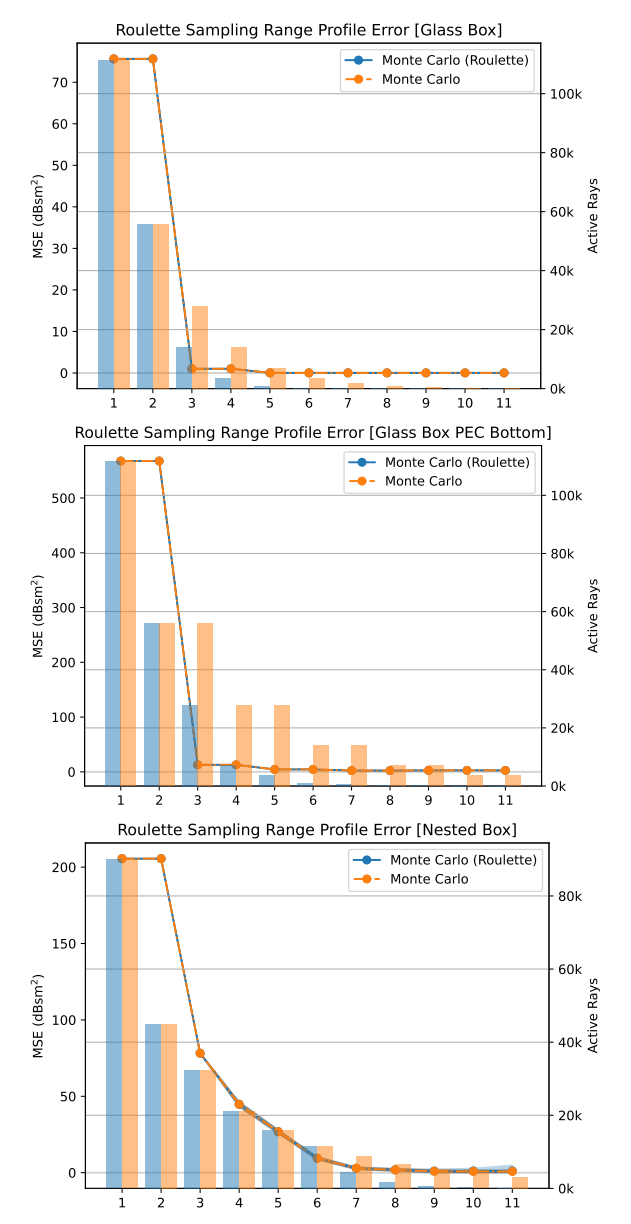


Fig. 11: Russian roulette sampling rapidly reduces active rays, halving them after the first bounce compared to full Monte Carlo. For single dielectric cubes, accuracy is maintained; for nested cubes, variance increases but remains controllable and often justified by the performance gain.

and the error by the line graphs. This figure compares the number of active rays at any given l in the path space with the corresponding error. We find that roulette sampling quickly decreases the number of rays after the initial cutoff. Within three bounces, our solver is able to stop while the deterministic method continues tracing rays until an overall maximum is reached. For the single dielectric blocks, we see no difference between the computed scattered fields and very little variance in the solution. The ray killing in the nested dielectrics introduces no bias for longer paths, but a slight increase in variance is found as expected. Russian roulette sampling along with the constant memory usage allows our method to easily compute long paths with limited computational overhead.

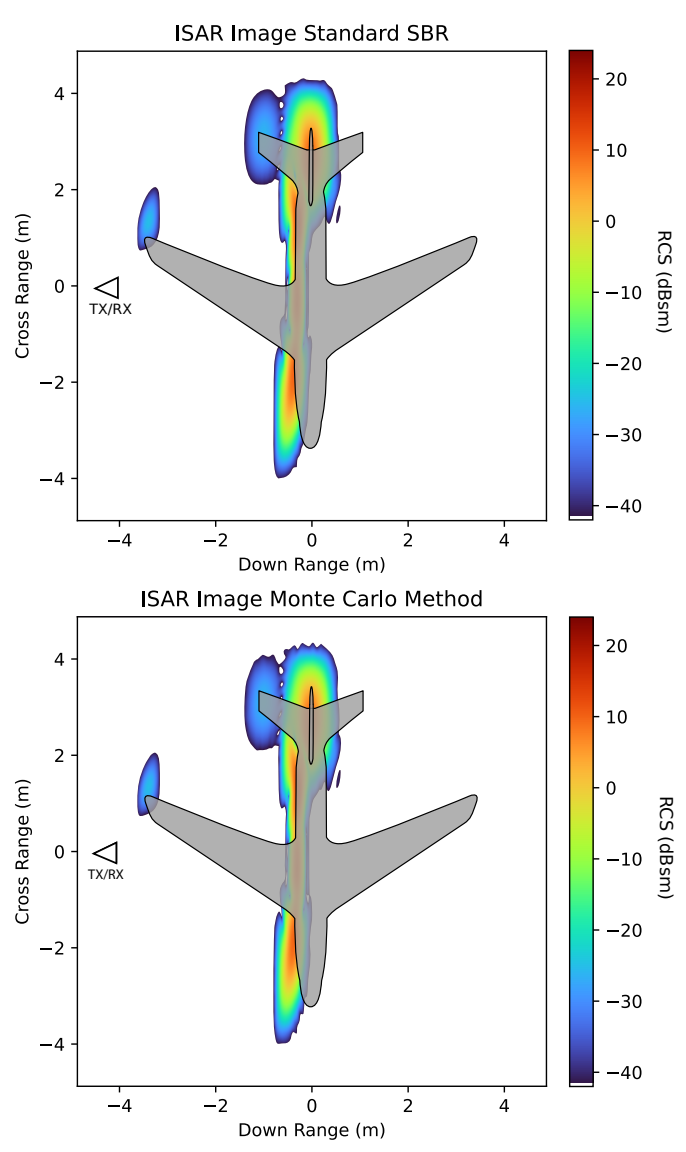


Fig. 12: Comparison of inverse synthetic aperture RADAR images for a PEC airplane using standard and Monte Carlo algorithms. Both methods accurately capture wing tip scattering and specular reflections, with no additional noise observed above the  $-40\ dB$  threshold. Results demonstrate the suitability of the Monte Carlo method for input to signal processing applications.

# E. Sensitivity to Noise

Monte Carlo integration makes higher dimensional integrals easier to compute at the cost of additional noise in the answer. Though real world systems expect noise in their result, if the noise produced by the numerical approximation is too high, then downstream signal processing can be corrupted. With sufficient sampling, we are able to get nulls at comparable levels to the classic SBR algorithm (Figures 5 and 6) in range profiles. To further demonstrate the applicability of our results to down stream tasks, we compare inverse synthetic aperture (ISAR) reconstructions [37] of the airplane model (Figure 9) to show that the noise in our results does not affect the reconstruction. ISARs are incredibly sensitive to

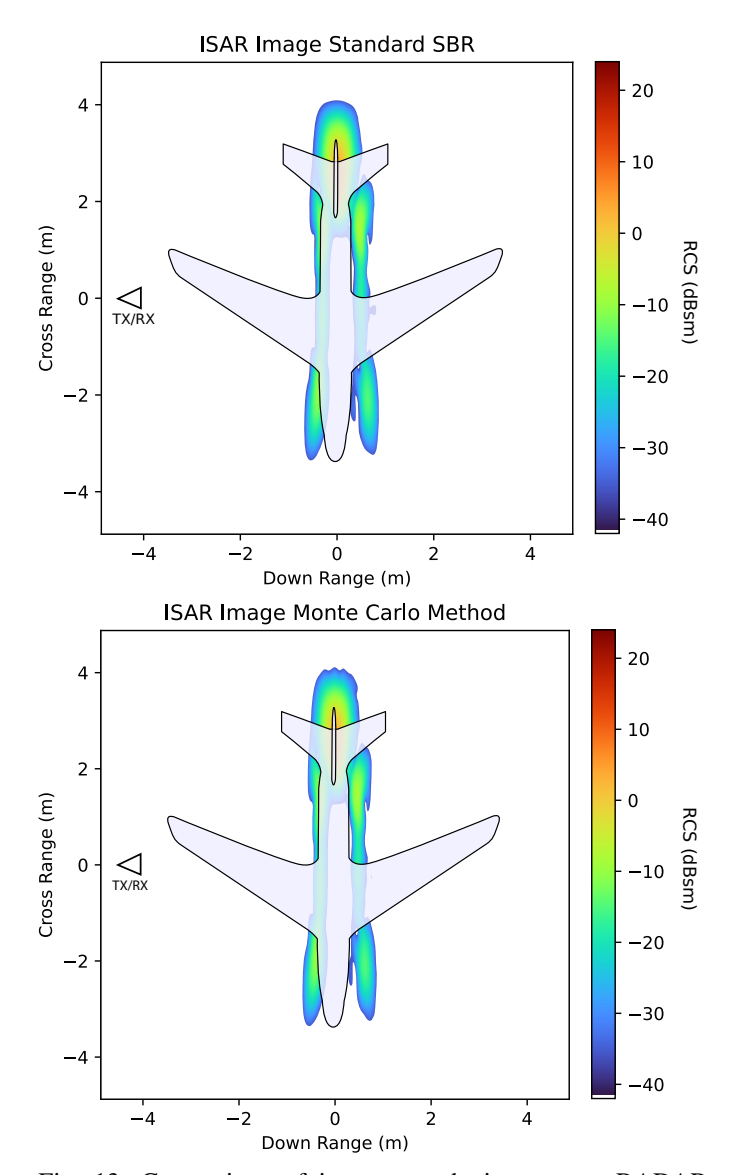


Fig. 13: Comparison of inverse synthetic aperture RADAR images for a dielectric airplane ( $\epsilon_r=1.5$ ) using standard and Monte Carlo algorithms. Both methods accurately capture specular reflections and wall scattering, with no additional noise above -40~dB in the Monte Carlo results. This demonstrates the suitability of the Monte Carlo method for downstream signal processing applications.

errors in phase, which will cause misplaced scatters which are no longer grounded to the underlying geometry. Figures 12 and 13 show that our method and the standard algorithm have similar performance with an effective ray density of 20. To match spacing in cross and down range, 130 frequencies from 1 to 3 GHz along 51 azimuthal angles from  $80^{\circ}$  to  $100^{\circ}$ . 3 bounces were used on the PEC geometry, while the max bounce was set to 5 for the dielectric plane. On PEC, we see that both methods produce ISARs that highlight the scattering off the wing tips and specular scattering off the fuselage and vertical stabilizer. No additional noise is found above the -40~dB level. Similar performance is found on the glass airplane geometry. We see that the specular along with

the opposite side scattering are captured by both techniques. For the PEC case, the runtime was roughly 5 minutes for both methods, while the dielectric plane took around 20 minutes in each. These results demonstrate that our method is suitable for traditional downstream tasks for scattered field simulations without onerous sampling requirements that would increase runtime over the deterministic algorithm.

Our results demonstrate that the Monte Carlo integration technique brings strong improvements to the SBR algorithm for complex geometries and difficult to calculate dielectric stack ups. Though performance is no better for simple shapes, our method uses an order of magnitude less memory and can be 4 times faster on objects containing multiple dielectric surfaces. We demonstrate additional performance improvements using common techniques from Monte Carlo based path tracing, but by no means have exhausted the extensive path tracing literature. Our results open up new domains for the SBR algorithm to compute scenes that are still too expensive for full wave solvers but require more fidelity than Geometric Optics provides on its own.

#### V. Conclusion

Our work extends the classic SBR algorithm to use Monte Carlo integration instead of poorly scaling quadrature rules. This change enables the SBR algorithm to compute scenes faster by decreasing ray trace calls and better aligning the algorithm with the underlying parallel hardware. Our results demonstrate this performance gain on dielectric blocks and nested material objects. The method does have limitations, and for simpler geometries, there is little benefit as runtimes are similar and noise is introduced. We also did not discuss inclusion of additional phenomenology like edge diffraction, cavity responses, or creeping waves. These are all deficiencies of the standard SBR algorithm but can be included in our method using existing techniques and superposition. In future work, higher order diffraction effects could even be easier to implement using our method. Another potential avenue is improved variance reduction techniques. We explored basic methods like stratified and Fresnel based importance sampling, but there is a long literature on Monte Carlo integration that could be leveraged. Notable methods are specular manifold importance sampling and control variates. Our method improves the scalability of the SBR algorithm while also enabling exciting avenues for future work leveraging techniques common in computer graphics.

#### ACKNOWLEDGMENT

The authors would like to thank Shayne Gerber, Dr. Leo Tchorowski, and Markus Ferrell for their feedback and comments on early drafts.

#### REFERENCES

[1] X. T. Nguyen, J. Hirokawa, M. Ando, O. Amano, T. Matsuzaki, S. Koreeda, and K. Takahashi, "A Method of Moments analysis and design of RLSA by using only a dominant mode basic function and correction length for slots," in 2013 Proceedings of the International Symposium on Antennas & Propagation, vol. 01, Oct. 2013, pp. 156–159. [Online]. Available: https://ieeexplore.ieee.org/abstract/document/6717400

- [2] J. Malmström and B. L. G. Jonssont, "An effective method for antenna placement on platforms based on the reaction theorem," in 2017 International Conference on Electromagnetics in Advanced Applications (ICEAA), Sep. 2017, pp. 1547–1550. [Online]. Available: https://ieeexplore.ieee.org/document/8065579
- [3] E. Whalen, A. Elfrgani, C. Reddy, and R. Rajan, "Antenna Placement Optimization for Vehicle-to-Vehicle Communications," in 2018 IEEE International Symposium on Antennas and Propagation & USNC/URSI National Radio Science Meeting, Jul. 2018, pp. 1673–1674, iSSN: 1947-1491. [Online]. Available: https://ieeexplore.ieee.org/document/8609047
- [4] J. Johnson and Y. Rahmat-Samii, "Genetic algorithms and method of moments (GA/MOM) for the design of integrated antennas," *IEEE Transactions on Antennas and Propagation*, vol. 47, no. 10, pp. 1606–1614, Oct. 1999, conference Name: IEEE Transactions on Antennas and Propagation. [Online]. Available: https://ieeexplore.ieee.org/document/805906
- [5] A. Di Serio, P. Hügler, F. Roos, and C. Waldschmidt, "2-D MIMO Radar: A Method for Array Performance Assessment and Design of a Planar Antenna Array," *IEEE Transactions on Antennas and Propagation*, vol. 68, no. 6, pp. 4604–4616, Jun. 2020, conference Name: IEEE Transactions on Antennas and Propagation. [Online]. Available: https://ieeexplore.ieee.org/abstract/document/9024239
- [6] Y. Liu, M. Ahmadi, J. Fuchs, M. Alaee-Kerahroodi, and M. R. Bhavani Shankar, "Dynamic Indoor mmWave MIMO Radar Simulation: An Image Rendering-Based Approach," *IEEE Transactions on Antennas and Propagation*, pp. 1–1, 2024, conference Name: IEEE Transactions on Antennas and Propagation. [Online]. Available: https://ieeexplore.ieee.org/document/10559769/?arnumber=10559769
- [7] J. Guan, S. Yan, and J.-M. Jin, "Electromagnetic simulation of specific absorption rate at 5G frequencies with a simplified human head model and a multi-solver method," in 2017 IEEE International Symposium on Antennas and Propagation & USNC/URSI National Radio Science Meeting, Jul. 2017, pp. 941–942, iSSN: 1947-1491. [Online]. Available: https://ieeexplore.ieee.org/document/8072513
- [8] R. F. Harrington, Field Computation by Moment Methods. Wiley-IEEE Press, 1993.
- [9] K. Yee and J. Chen, "The finite-difference time-domain (FDTD) and the finite-volume time-domain (FVTD) methods in solving Maxwell's equations," *IEEE Transactions on Antennas and Propagation*, vol. 45, no. 3, pp. 354–363, Mar. 1997, conference Name: IEEE Transactions on Antennas and Propagation. [Online]. Available: https://ieeexplore.ieee.org/document/558651
- [10] J.-M. Jin, Z. Lou, Y.-J. Li, N. W. Riley, and D. J. Riley, "Finite Element Analysis of Complex Antennas and Arrays," *IEEE Transactions on Antennas and Propagation*, vol. 56, no. 8, pp. 2222–2240, Aug. 2008, conference Name: IEEE Transactions on Antennas and Propagation. [Online]. Available: https://ieeexplore.ieee.org/document/4589110
- [11] P. H. Pathak and R. J. Burkholder, Electromagnetic Radiation, Scattering, and Diffraction, 1st ed., ser. IEEE Press. Wiley-IEEE Press, 2022.
- [12] H. Ling, R.-C. Chou, and S.-W. Lee, "Shooting and bouncing rays: calculating the RCS of an arbitrarily shaped cavity," *IEEE Transactions on Antennas and Propagation*, vol. 37, no. 2, pp. 194–205, Feb. 1989, conference Name: IEEE Transactions on Antennas and Propagation. [Online]. Available: https://ieeexplore.ieee.org/document/18706
- [13] R. Brem and T. F. Eibert, "A Shooting and Bouncing Ray (SBR) Modeling Framework Involving Dielectrics and Perfect Conductors," *IEEE Transactions on Antennas and Propagation*, vol. 63, no. 8, pp. 3599–3609, Aug. 2015, conference Name: IEEE Transactions on Antennas and Propagation. [Online]. Available: https://ieeexplore.ieee.org/abstract/document/7114218
- [14] C. Y. Kee and C.-F. Wang, "Efficient GPU Implementation of the High-Frequency SBR-PO Method," *IEEE Antennas and Wireless Propagation Letters*, vol. 12, pp. 941–944, 2013. [Online]. Available: https://ieeexplore.ieee.org/document/6568879
- [15] Y. Kim, H. Yang, H. Kim, J. Jo, and J. Oh, "Anxel Beam Shrinkage Method and Heterogeneous Computing-Accelerated Full-Image Theory Method Ray Tracing Enabling Massive Outdoor Propagation Modeling," *IEEE Transactions on Antennas and Propagation*, vol. 72, no. 7, pp. 5935–5949, Jul. 2024. [Online]. Available: https://ieeexplore.ieee.org/document/10558764
- [16] S. Kasdorf, B. Troksa, C. Key, J. Harmon, and B. M. Notaroš, "Advancing Accuracy of Shooting and Bouncing Rays Method for Ray-Tracing Propagation Modeling Based on Novel Approaches to Ray Cone Angle Calculation," *IEEE Transactions on Antennas and Propagation*, vol. 69, no. 8, pp. 4808–4815, Aug. 2021. [Online]. Available: https://ieeexplore.ieee.org/document/9362202

- [17] Z. Yun and M. F. Iskander, "Ray Tracing for Radio Propagation Modeling: Principles and Applications," *IEEE Access*, vol. 3, pp. 1089–1100, 2015. [Online]. Available: https://ieeexplore.ieee.org/document/7152831
- [18] M. Pharr, W. Jakob, and G. Humphreys, Physically Based Rendering: From Theory to Implementation (3rd ed.), 3rd ed. San Francisco, CA, USA: Morgan Kaufmann Publishers Inc., Oct. 2016.
- [19] J. T. Kajiya, "The rendering equation," SIGGRAPH Comput. Graph., vol. 20, no. 4, pp. 143–150, Aug. 1986. [Online]. Available: https://dl.acm.org/doi/10.1145/15886.15902
- [20] E. Veach and L. J. Guibas, "Metropolis light transport," in *Proceedings of the 24th annual conference on Computer graphics and interactive techniques*, ser. SIGGRAPH '97. USA: ACM Press/Addison-Wesley Publishing Co., Aug. 1997, pp. 65–76. [Online]. Available: https://dl.acm.org/doi/10.1145/258734.258775
- [21] R. Wang and D. Manocha, "Dynamic Coherence-Based EM Ray Tracing Simulations in Vehicular Environments," in 2022 IEEE 95th Vehicular Technology Conference: (VTC2022-Spring), Jun. 2022, pp. 1–7, iSSN: 2577-2465. [Online]. Available: https://ieeexplore.ieee.org/document/9860362
- [22] P. Peng and G. Lixin, "A New Shooting Bouncing Ray Method for Composite Scattering from a Target above the Electrically Large Scope Sea Surface," *Mathematical Problems* in Engineering, vol. 2017, no. 1, p. 6201745, 2017, \_eprint: https://onlinelibrary.wiley.com/doi/pdf/10.1155/2017/6201745. [Online]. Available: https://onlinelibrary.wiley.com/doi/abs/10.1155/2017/6201745
- [23] M. Born and E. Wolf, Principles of optics: 60th anniversary edition, 7th ed. Cambridge, England: Cambridge University Press, 2019.
- [24] J. G. Meana, J. A. Martínez-Lorenzo, C. Rappaport, and F. Las-Heras, "Modified Equivalent Current Approximation (MECA) applied to radioelectric coverage evaluation in rural scenarios," in *Proceedings of* the Fourth European Conference on Antennas and Propagation, Apr. 2010, pp. 1–4, iSSN: 2164-3342. [Online]. Available: https://ieeexplore.ieee.org/document/5505411
- [25] L. Zhang, Z. Hou, C. Wang, and H. Yin, "Extended Modified Equivalent Current Approximation Method for Pure or Low Lossy Dielectric Objects," in 2015 IEEE 12th Intl Conf on Ubiquitous Intelligence and Computing and 2015 IEEE 12th Intl Conf on Autonomic and Trusted Computing and 2015 IEEE 15th Intl Conf on Scalable Computing and Communications and Its Associated Workshops (UIC-ATC-ScalCom), Aug. 2015, pp. 1607–1610. [Online]. Available: https://ieeexplore.ieee.org/document/7518473
- [26] J.-M. Jin, "Electromagnetic Theorems and Principles," in Theory and Computation of Electromagnetic Fields. John Wiley & Sons, Ltd, 2010, pp. 73–106. [Online]. Available: https://onlinelibrary.wiley.com/doi/abs/10.1002/9780470874257.ch3
- [27] A. Burden, R. Burden, and J. D. Faires, *Numerical Analysis*, 10th ed. Mason, OH: CENGAGE Learning Custom Publishing, 2015.
- [28] J. L. Bentley, "Multidimensional binary search trees used for associative searching," *Commun. ACM*, vol. 18, no. 9, pp. 509–517, Sep. 1975. [Online]. Available: https://dl.acm.org/doi/10.1145/361002.361007
- [29] D. Meister, S. Ogaki, C. Benthin, M. J. Doyle, M. Guthe, and J. Bittner, "A Survey on Bounding Volume Hierarchies for Ray Tracing," Computer Graphics Forum, vol. 40, no. 2, pp. 683–712, 2021, \_eprint: https://onlinelibrary.wiley.com/doi/pdf/10.1111/cgf.142662. [Online]. Available: https://onlinelibrary.wiley.com/doi/abs/10.1111/cgf.142662
- [30] W. Jakob, S. Speierer, N. Roussel, M. Nimier-David, D. Vicini, T. Zeltner, B. Nicolet, M. Crespo, V. Leroy, and Z. Zhang, "Mitsuba 3 renderer," 2022.
- [31] T. Zeltner, I. Georgiev, and W. Jakob, "Specular manifold sampling for rendering high-frequency caustics and glints," ACM Trans. Graph., vol. 39, no. 4, pp. 149:149:1-149:15, Aug. 2020. [Online]. Available: https://doi.org/10.1145/3386569.3392408
- [32] I. Guillén, J. Marco, D. Gutierrez, W. Jakob, and A. Jarabo, "A general framework for pearlescent materials," ACM Trans. Graph., vol. 39, no. 6, pp. 253:1–253:15, Nov. 2020. [Online]. Available: https://dl.acm.org/doi/10.1145/3414685.3417782
- [33] B. Nicolet, F. Rousselle, J. Novak, A. Keller, W. Jakob, and T. Müller, "Recursive Control Variates for Inverse Rendering," ACM Trans. Graph., vol. 42, no. 4, pp. 62:1–62:13, Jul. 2023. [Online]. Available: https://doi.org/10.1145/3592139
- [34] W. Jakob, S. Speierer, N. Roussel, and D. Vicini, "DR.JIT: a just-in-time compiler for differentiable rendering," ACM Trans. Graph., vol. 41, no. 4, pp. 124:1–124:19, Jul. 2022. [Online]. Available: https://doi.org/10.1145/3528223.3530099
- [35] J. Nickolls, I. Buck, M. Garland, and K. Skadron, "Scalable Parallel Programming with CUDA: Is CUDA the parallel programming

- model that application developers have been waiting for?" *Queue*, vol. 6, no. 2, pp. 40–53, Mar. 2008. [Online]. Available: https://dl.acm.org/doi/10.1145/1365490.1365500
- [36] S. G. Parker, J. Bigler, A. Dietrich, H. Friedrich, J. Hoberock, D. Luebke, D. McAllister, M. McGuire, K. Morley, A. Robison, and M. Stich, "OptiX: a general purpose ray tracing engine," ACM Trans. Graph., vol. 29, no. 4, pp. 66:1–66:13, Jul. 2010. [Online]. Available: https://doi.org/10.1145/1778765.1778803
- [37] V. C. Chen and M. Martorella, Inverse Synthetic Aperture Radar Imaging: Principles, algorithms and applications. Norwich, CT: SciTech Publishing, 2014.

Samuel Audia Samuel Audia is a PhD student at the University of Maryland, College Park in the departmente of Computer Science. He previously received BSc's in Computer Science and Mechanical Engineering from the University of Maryland, College Park. Sam also has a MSc from Johns Hopkins University in Applied and Computational Mathematics. His research focuses on improving computational electromagnetic simulations using methods from machine learning and computer graphics.

Dinesh Manocha Dinesh Manocha is a Distinguished University Professor at the University of Maryland and Paul Chrisman Iribe Professor of Computer Science and Electrical and Computer Engineering. He is also the Phi Delta Theta/Matthew Mason Distinguished Professor Emeritus of Computer Science at Chapel Hill University of North Carolina. Mancha's research focuses on AI, robotics, computer graphics, augmented/virtual reality, and scientific computing, and has published more than 730 papers (H-index 135). He has supervised 46 PhD dissertations, and his group has won 21 best paper awards at leading conferences. His group has developed many widely used software systems (with 500K+ downloads) and licensed them to more than 60 commercial vendors. He is an inventor of 16 patents, several of which have been licensed to industry. A Fellow of AAAI, AAAS, ACM, IEEE and Sloan Foundation, Manocha is a ACM SIGGRAPH Academy Class member and Bézier Award recipient from Solid Modeling Association. He received the Distinguished Alumni Award from IIT Delhi and the Distinguished Career in Computer Science Award from Washington Academy of Sciences. He was also the co-founder of Impulsonic, a developer of physics-based audio simulation technologies, which Valve Inc. acquired in November 2016. He is also a cofounder of Inception Robotics, Inc.

Matthias Zwicker Matthias Zwicker is the Elizabeth Iribe Chair for Innovation and the Phillip H. and Catherine C. Horvitz Professor of Computer Science, and currently serves as the Chair of the Department of Computer Science at UMD. He joined UMD in March 2017 as the Reginald Allan Hahne Endowed E-Nnovate Professor in Computer Science. He obtained his PhD from ETH in Zurich, Switzerland, in 2003. From 2003 to 2006 he was a post-doctoral associate with the computer graphics group at the Massachusetts Institute of Technology, and then held a position as an Assistant Professor at the University of California in San Diego from 2006 to 2008. From 2008-2017, he was a professor in Computer Science at the University of Bern, Switzerland, where he served as the head of the Computer Graphics Group and as director of undergraduate and graduate studies. His research focus is on the intersection of artificial intelligence and computer graphics. with the goal of enabling next generation AR/VR and computer graphics applications. He has served as a papers co-chair and conference chair of the IEEE/Eurographics Symposium on Point-Based Graphics, and as a papers cochair for Eurographics and the Eurographics Symposium on Rendering. He has been a member of program committees for various conferences including ACM SIGGRAPH, ACM SIGGRAPH Asia, and Eurographics, and he has served as an associate editor for journals such as the Computer Graphics Forum, IEEE TVCG, and the Visual Computer. As an active member of the UMD community, he has served as a University Senator for the CS department, as a faculty co-lead in developing the new Immersive Media Design major, and as a faculty mentor in the Gemstone Honors Program.